Seismotectonic Analysis of the 2019–2020 Puerto Rico Sequence: The Value of Absolute Earthquake Relocations in Improved Interpretations of Active Tectonics

Copeland W. Cromwell*[1], Kevin P. Furlong[1], Eric A. Bergman[2], Harley M. Benz[3], Will L. Yeck[3], and Matthew Herman[4]

Abstract

We present a new catalog of calibrated earthquake relocations from the 2019–2020 Puerto Rico earthquake sequence related to the 7 January 2020 M_w 6.4 earthquake that occurred offshore of southwest Puerto Rico at a depth of 15.9 km. Utilizing these relocated earthquakes and associated moment tensor solutions, we can delineate several distinct fault systems that were activated during the sequence and show that the M_w 6.4 mainshock may have resulted from positive changes in Coulomb stress from earlier events. Seismicity and mechanisms define (1) a west–southwest (~260°) zone of seismicity comprised of largely sinistral strike-slip and oblique-slip earthquakes that mostly occurs later in the sequence and to the west of the mainshock, (2) an area of extensional faulting that includes the mainshock and occurs largely within the mainshock's rupture area, and (3) an north–northeast (~30°)-striking zone of seismicity, consisting primarily of dextral strike-slip events that occurs before and following the mainshock and generally above (shallower than) the normal-faulting events. These linear features intersect within the M_w 6.4 mainshock's fault plane in southwest Puerto Rico. In addition, we show that earthquake relocations for M 4+ normal-faulting events, when traced along their fault planes, daylight along east–west-trending bathymetric features offshore of southwest Puerto Rico. Correlation of these normal-faulting events with bathymetric features suggests an active fault system that may be a contributor to previously uncharacterized seismic hazards in southwest Puerto Rico.

Cite this article as Cromwell, C. W., K. P. Furlong, E. A. Bergman, H. M. Benz, W. L. Yeck, and M. Herman (2021). Seismotectonic Analysis of the 2019–2020 Puerto Rico Sequence: The Value of Absolute Earthquake Relocations in Improved Interpretations of Active Tectonics, *Seismol. Res. Lett.* **93**, 544–554, doi: 10.1785/0220210238.

Supplemental Material

Tectonic Background

Puerto Rico is located within a ~350-km-wide deformation zone along the northeastern boundary of the Caribbean (CA) plate (Prentice and Mann, 2005; Roig-Silva *et al.*, 2013). This deformation zone is separated from the North American (NA) plate on the north by the east–west-striking Puerto Rico trench. Here, oblique subduction results in the southwestern underthrusting of the NA plate beneath the CA plate at a rate of ~20 mm/yr (DeMets *et al.*, 2010) with the underthrust NA plate extending up to 150 km beneath Puerto Rico (McCann, 1985). This oblique subduction becomes pure strike-slip farther west (Byrne *et al.*, 1985). In the south, Puerto Rico is bound by the Muertos trough (Clinton *et al.*, 2006); a deep eastward narrowing submarine canyon (Granja Bruña *et al.*, 2009), which has been interpreted as a trench associated with CA plate subducting beneath a Puerto Rican microplate (Byrne *et al.*, 1985; McCann, 1985). However, the lack of a clear Wadati–Benioff zone (Dolan *et al.*, 1998; Mann *et al.*, 2002; Granja Bruña *et al.*, 2009) makes it difficult to reconcile the importance of the Muertos trough in terms of a seismotectonic framework and implication for long-term seismic hazards.

To the east and west, Puerto Rico is bounded by broad zones of active extension in the Anegada trough and Mona Canyon, respectively (Prentice and Mann, 2005; Clinton *et al.*,

1. Department of Geosciences, Pennsylvania State University, University Park, Pennsylvania, U.S.A., https://orcid.org/0000-0002-2674-5110 (KPF); 2. Global Seismological Services, Golden, Colorado, U.S.A.; 3. United States Geological Survey, Denver, Colorado, U.S.A., https://orcid.org/0000-0002-2801-8873 (WLY); 4. Department of Geological Sciences, California State University-Bakersfield, Bakersfield, California, U.S.A., https://orcid.org/0000-0003-4684-9459 (MH)

*Corresponding author: cwc5778@psu.edu

© Seismological Society of America

Downloaded from http://pubs.geoscienceworld.org/ssa/srl/article-pdf/93/2A/544/5553020/srl-2021238.1.pdf
by USGS Library user

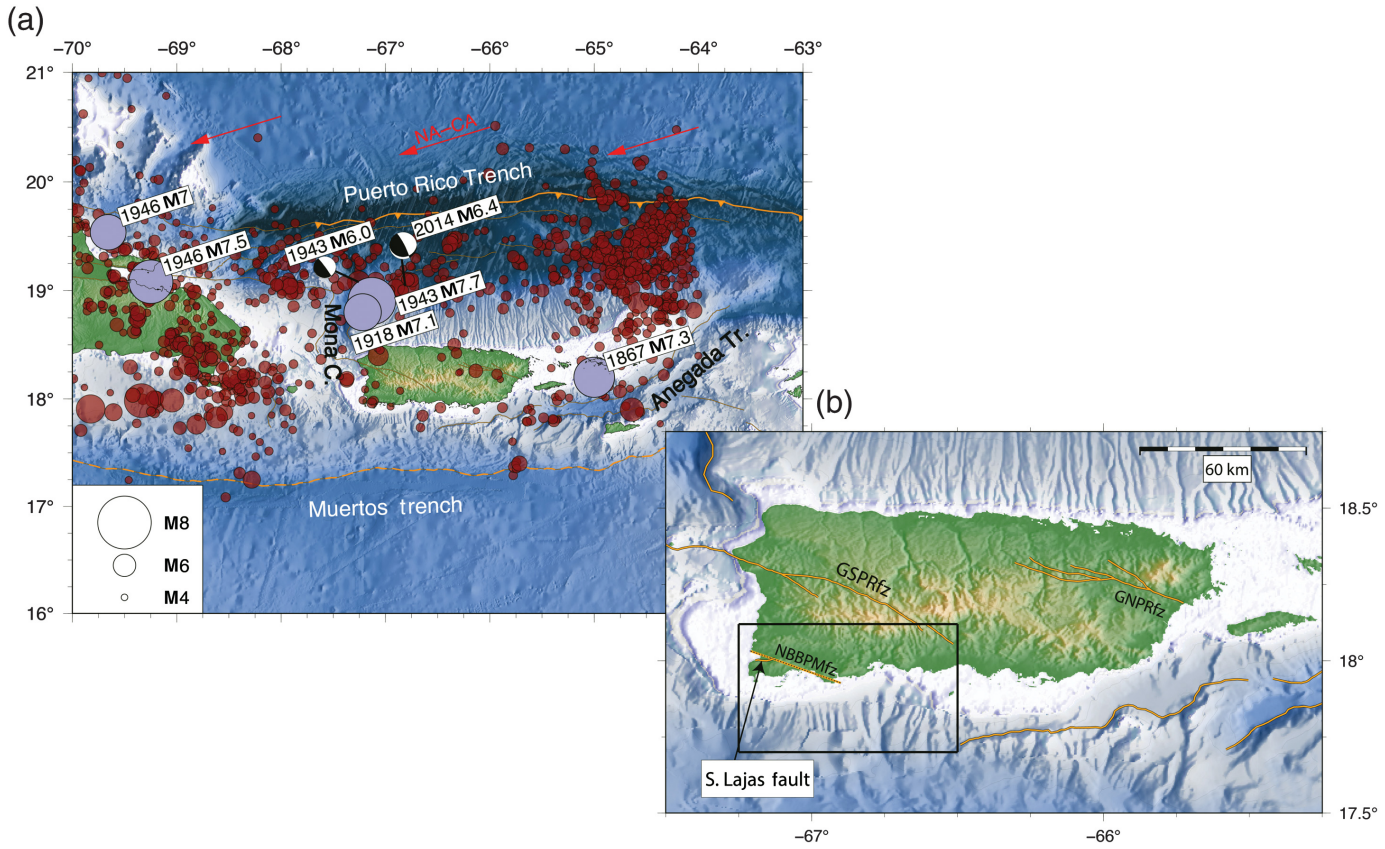


Figure 1. (a) Mid-ocean ridge velocity plate motions showing the oblique North American (NA)–Caribbean (CA) plate motions along the Puerto Rico trench. **M** 7+ seismicity for the past 200 yr is shown occurring primarily to the north and west of Puerto Rico in purple with no **M** 7+ occurring onshore. **M** 4+ events from 1969–2019 are shown in red. The 13 January 2014 M_w 6.4 and 3 November 1988 **M** 6.0 thrust faulting events are shown as black focal mechanisms. Seismicity primarily occurs along the north of the island and offshore with seismicity in southwest Puerto Rico being sparse throughout the recorded period with no **M** 5+ events recorded prior to December 2019. (b) The black box shows the extent of the study area and relocated events in this work. The Great Southern Puerto Rico fault zone (GSPRfz), Great North Puerto Rico fault zone (GNPRfz), the South Lajas fault, and the north Boquerón Bay–Punta Montalva fault zone (NBBPMfz) are labeled for reference. Compiled faults and plate boundaries were accessed from Styron *et al.* (2020). The NBBPMfz is from Roig-Silva *et al.* (2013). Earthquake locations and mechanisms are from the U.S. Geological Survey Advanced National Seismic System (USGS ANSS) Comprehensive Earthquake Catalog (ComCat), which provides preferred locations that are generally either National Earthquake Information Center or the Puerto Rico seismic network.

2006). The Mona Canyon and Anegada trough have each hosted damaging **M** 7+ earthquakes, including the tsunamigenic events in 1918 and 1867 (McCann, 1985). The location of these **M** 7+ earthquakes is shown in Figure 1a. In addition to these offshore systems, numerous onshore fault systems, such as the South Lajas fault (Prentice and Mann, 2005) and Great Southern Puerto Rico fault zone (van Gestel *et al.*, 1998) have been identified and are considered to pose earthquake hazards in Puerto Rico. Recent work has shown the presence of the seismically active onshore North Boquerón Bay–Punta Montalva fault zone (NBBPMfz) which begins north of and intersects the South Lajas fault (Fig. 1b). The NBBPMfz hosts primarily left-lateral and smaller northeast-striking normal-faulting events (Roig-Silva *et al.*, 2013; M. Blasweiler *et al.*, unpublished manuscript, see Data and Resources). The location of the island of Puerto Rico within this tectonically complex zone of deformation has subjected it to numerous damaging earthquakes and tsunamis throughout its recorded history (Clinton *et al.*, 2006; Mueller *et al.*, 2010). However, as discussed in the following, virtually all significant earthquake activity has occurred offshore Puerto Rico (Fig. 1a).

Seismicity surrounding Puerto Rico is dominated by small offshore events (Jansma and Mattioli, 2005), and occasional steeply dipping **M** 6+ thrust events, with slip occurring (~230° azimuth) in a similar orientation to plate motions (~250°) (e.g., 3 November 1988 **M** 6.0 and the 13 January 2014 M_w 6.4 events shown as focal mechanisms in Fig. 1a). Historically, larger **M** 7+ events have occurred to the northwest and east of the island of Puerto Rico (Prentice and Mann, 2005), distant from coastlines (McCann, 2002). The locations of these large historic events are shown in Figure 1a (from the U.S. Geological Survey [USGS] Comprehensive Earthquake Catalog

Downloaded from http://pubs.geoscienceworld.org/ssa/srl/article-pdf/93/2A/544/5553020/srl-2021238.1.pdf
by USGS Library user

[ComCat]). In addition, small (**M** <3) onshore seismic events are common in Puerto Rico and may be resultant from upper plate deformation or the interaction of onshore faults such as the South Lajas fault and are primarily characterized by strike-slip and extensional faulting (Prentice and Mann, 2005). Although larger earthquakes (**M** 5+) are common along the Puerto Rico trench, larger events like the 7 January 2020 M_w 6.4 and associated seismicity of the 2019–2020 southwest Puerto Rico seismic sequence (SWPRSS) have not been previously observed.

Calibrated Relocations

The earthquakes relocated in this study were initially taken from the International Seismological Centre (ISC) Bulletin by searching a radius of 50 km from the 7 January 2020 M_w 6.4 USGS National Earthquake Information Center (NEIC) location for the period 28 December 2019–04 July 2020. Importantly, the ISC Bulletin contains earthquake source parameters provided by USGS NEIC, which includes arrival-time data from the important temporary, local, and regional stations. The assembled dataset includes 200 earthquakes with 40 or more arrival-time readings; it is composed of 22 foreshocks, the mainshock, and 177 aftershocks. Most events have magnitude 3.5 or larger and many are recorded to teleseismic distances.

The hypocenters (latitude, longitude, depth, and origin time) of the SWPRSS were computed using a multiple event relocation algorithm that has been developed to produce "calibrated" locations with suitable datasets. The method and procedures used here follow those found in Gaudreau *et al.* (2019), Nissen *et al.* (2019), and Soto Cordero *et al.* (2020). The study of Soto Cordero *et al.* (2020) has similarities to this work with both onshore and offshore earthquakes in the sequence.

Calibrated earthquake locations have the characteristic that location bias from unknown Earth structure is minimized, and their uncertainties can be taken as realistic and not purely model-based. The key to more accurate estimates of hypocentral parameter uncertainties is the estimation of data variance, as derived empirically from the arrival-time data itself, for each multiply observed station-phase pair. This drives a statistically significant identification of outlier readings, which are deleted when locating earthquakes. Data are weighted inversely to their empirically derived variances.

Calibration of the SWPRSS was done using "direct calibration" in which the hypocentroid of the cluster (a virtual event at the geometric mean of all hypocentral coordinates) is located using near-source (0°–1°) arrival-time data from all 200 events. This implies that only stations within the Puerto Rico network (5058 arrival times) were used in assessing the hypocentroid, which establishes the absolute location of each event in the sequence. The relative locations (cluster vectors) are computed using multiply observed station-phase arrivals at all distances (23,201) for which a phase identification is possible, and for which a theoretical travel time can be calculated using the reference earth model, *ak135* (Kennett *et al.*, 1995).

TABLE 1
Crustal Model for the 2019–2020 Southwest Puerto Rico Seismic Sequence Calibrated Relocations

Thickness (km)	*P* Velocity (km/s)	*S* Velocity (km/s)
0–10	5.0	3.0
10–20	5.8	3.46
20-45	6.0	4.0
45+	8.04	4.55

An important aspect of the calibration process is the development of a crustal velocity model (1D) that produces estimates of theoretical travel time that are consistent with the observed arrival times over the distance range used to estimate the hypocentroid. Initially, a cluster of events in the interior of the island that have excellent azimuthal coverage and good depth control from close stations are used to determine a velocity model. Because more events with good azimuthal coverage and depth control are added, adjustments are made accordingly. In all, a dozen or so iterations are done to refine the crustal model, which has the characteristic of near zero mean *Pg*- and *Sg*-arrival-time residuals (Fig. S1).

After the crustal velocity model is converged, the thickness of the crust (Moho depth) is adjusted to match the more distant *Pn* and *Sn* observations. The resulting crustal model for a cluster of events in the SWPRSS is given in Table 1. Theoretical travel times of phases other than the crustal direct arrivals *Pg* and *Sg* and the Moho-refracted arrivals *Pn* and *Sn* are calculated with *ak135*. Baseline offsets (Fig. S1) and other issues are factored in when computing the cluster vectors, which minimizes the need for complex velocity models.

Relocation of the SWPRSS cluster is potentially problematic because of poor azimuthal coverage at close distances, that is, most stations lie north of the offshore seismicity. This is partially offset by the abundance of *Sg* readings for all events. We investigated this issue by calibrating a separate cluster composed mainly of events in the interior of the island with excellent azimuthal coverage, to which we added the 7 January 2020 M_w 6.4 earthquake. This reference cluster required a slightly different crustal velocity model to optimally fit the observations, and some of the near-source readings for the M_w 6.4 earthquake were not well matched by it. However, this gave us a reference location for comparison with the location of the mainshock when it was relocated in the context of the foreshock–aftershock sequence (with its own preferred crustal model). Our final location places the mainshock ~1.5 km north of the reference location and ~1.5 km shallower. Given the differences in datasets, assumed crustal models, and formal uncertainties in both relocations, this represents an encouraging level of agreement. Figure S2 shows the distribution of all the stations used in relocating the SWPRSS. The figure shows good azimuthal coverage

Downloaded from http://pubs.geoscienceworld.org/ssa/srl/article-pdf/93/2A/544/5553020/srl-2021238.1.pdf
by USGS Library user

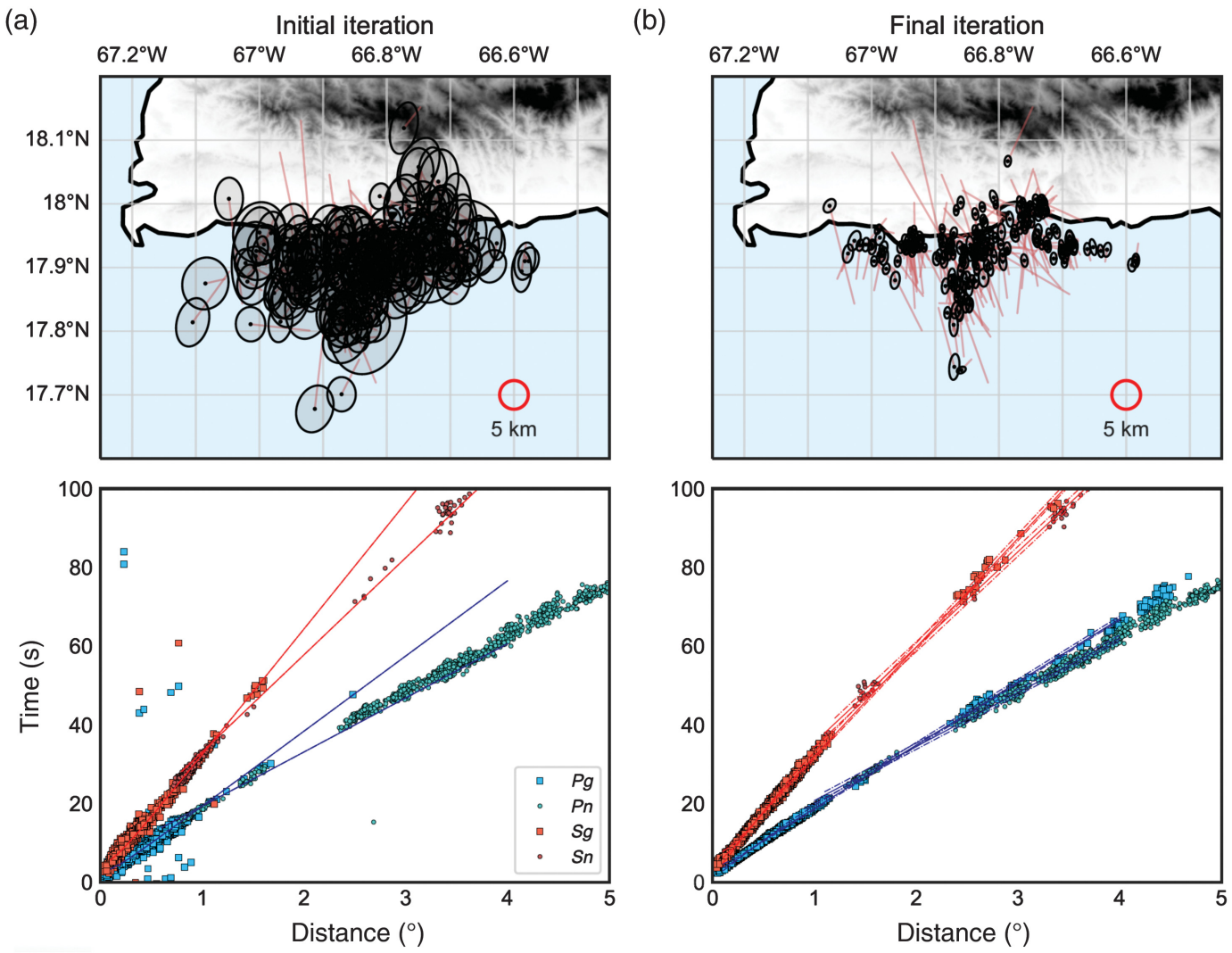


Figure 2. Initial and final locations of a calibrated cluster of earthquakes for 2019–2020 southwest Puerto Rico seismic sequence. (a) The results of the first run in which all data are weighted equally; focal depths are taken from the input data files (International Seismological Centre [ISC]); the crustal model has not yet been refined. The change in location from initial locations (ISC) are shown by red vectors. The confidence ellipse (90%) for each event is for the relative location only; the uncertainty of the hypocentroid that defines the absolute location is shown by the blue ellipse. The uncertainty of the hypocentroid must be added to the uncertainty of relative location to obtain the uncertainty of absolute location for any given event. A red circle of 5 km radius is shown for scale. (b) The final relocation is shown after refinement of the crustal velocity model and focal depths, determination of empirical reading errors for each station-phase, identification and flagging of outliers based on the empirical reading errors. There are dozens of runs in between panels (a) and (b). Some events may have been dropped if they could not be located.

with significant numbers of observations at local and regional teleseismic distances.

The specification of uncertainty for hypocentral parameters presents a choice between the uncertainty of relative locations and that of absolute locations, which are inflated to some extent by the uncertainty of the hypocentroid. For example, the epicentral uncertainty (semimajor axis length of the 90% confidence ellipse) for the mainshock in relative terms is 0.5 km, but it is 1.4 km in absolute terms. For comparing seismicity with geographic features, the absolute uncertainty is clearly preferred, but relative uncertainties may be preferred for some types of interpretation. The uncertainty in all cases is greatest in the north–south direction because of the weak azimuthal coverage. Figure 2 shows the evolution of the processing from beginning iterations that considers all available data with appropriate outlier removal to the final iteration that appropriately statistical weighting based on station-phase pairs. Initial absolute uncertainties (90% confidence, semimajor axis) for the whole dataset are 7.45 km, whereas the final absolute uncertainties (90% confidence, semimajor axis) are 2.18 km (Fig. S3).

Because of the richness of near-source arrival-time observations, the relocation could be done with focal depth as a free parameter for all 200 events, with uncertainties (for absolute

Downloaded from http://pubs.geoscienceworld.org/ssa/srl/article-pdf/93/2A/544/5553020/srl-2021238.1.pdf
by USGS Library user

location, 90%) in the range 0.6–1.3 km with a mode of 0.8 km. Depths range from 9 to 23 km with a concentration between 13 and 18 km. The mainshock's focal depth is 15.9 ± 0.6 km.

Moment Tensor Solutions

The moment tensor solutions used in this study were computed either using the *W*-phase method for the larger events (Hayes *et al.*, 2009) or a regional moment tensor (RMT) method (Herrmann *et al.*, 2011). Both are computed by NEIC staff and are available in the USGS ComCat (Data and Resources). In general, the *W*-phase mechanism was preferred for the **M** 5 or larger events, whereas the RMT solution was preferred for the smaller events. All but two of the **M** 5 or larger events in this study had a *W*-phase solution. The two **M** 5 or larger events without a moment tensor solution were aftershocks following closely in time to a large event. Of the 108 **M** 4 or larger events in this dataset, 23 *W* phase and 83 RMTs were computed. The number of RMTs solutions computed falls off significantly for events smaller than **M** 4 because of poor signal-to-noise ratio as many stations. *W*-phase and RMT modeling produced similar mechanisms for most events in which both methods were used. *W*-phase filtering was generally done in the 50–150 s passband. RMT processing for events lower than **M** 4 was typically filtered in the 16–50 s passband, whereas larger events used a passband filter of 20–50 s.

NEIC RMT solutions for which we have the most moment tensor solutions use all observational data in the distance range 0–500 km, but given the island setting observations were generally restricted to distances of less than 100 km. RMT solutions were computed using the western U.S. velocity model (Herrmann *et al.*, 2011) and three-component waveforms that included the complete body waves and surface waves. Moment tensor modeling is done at sufficiently long periods to minimize velocity model and location effects on the estimate of the moment and mechanism. Constraints on both the moment and radiation pattern are primarily provided by surface waves. The western U.S. velocity model was used because it is one of the operational models used by the NEIC and it provided consistent phase matching between the long-period body waves and surface waves. The velocity model's most significant contribution will be on the estimated depth of the best-fit RMT solutions. Likewise, the moment tensor solutions are minimally affected by the initial locations. The preferred RMT and *W*-phase solution for each event was the one with the best fit as a function of depth. The fit function was a weighted vector dot product that is equivalent to a reduction of variance, which is also normalized to give a value between 0% and 100%. Comparable mechanisms and moment magnitudes (within ±0.15 magnitudes) were found for events with both a *W*-phase and RMT solution. This study did not attempt to compute a local velocity model and associated Green's functions because the authors felt the resulting moment tensor solutions would not alter the understanding of the sequence.

December 2019–January 2020 Earthquake Sequence

The location of the 2019–2020 earthquake sequence is in an area that has previously experienced little significant seismicity (Fig. 1a). Interestingly, the SWPRSS shows significant changes in the style of faulting and orientation of seismicity (Fig. 3). Figure 3 shows a systematic migration of relocated seismicity northward by several kilometers and a better alignment of seismicity into distinct fault systems. Within the sequence there are numerous strike-slip and normal-faulting earthquakes, and oblique events intermediate between the two (Fig. 4 ternary diagram). We identify three distinct trends: A ∼30° north–northeast-trending group of earthquakes comprised largely of right-lateral strike-slip events, a ∼260° west–southwest-trending sequence of left-lateral strike-slip events, and a set of deeper normal-faulting events (Fig. 5).

The earthquake sequence from 28 December 2019, until 20 January 2020, shows distinct rupture characteristics surrounding the mainshock. Beginning 28 December 2019, and prior to the 7 January 2020, mainshock events are exclusively strike-slip events as can be seen in Figure 4. Large foreshocks, such as the 29 December 2019 M_w 4.8 and the 06 January 2020 M_w 5.7 and M_w 4.8 events, consistently indicate fault-plane strikes of 20°–30° with preferred nodal planes aligning along a linear north–northeastern-trending line, indicating right-lateral strike-slip motion. The events aligned along this north–northeastern trend exhibit little oblique slip (blue events of the ternary classification of Fig. 4). These earthquakes yield consistent and steeply dipping fault planes (∼80°) and rakes (∼−170°) consistent with almost pure strike-slip motion and may have occurred along the eastern portion of the NBBPMfz (M. Blasweiler *et al.*, unpublished manuscript, see Data and Resources). Two of these events, the M_w 4.8 and 5.7 right-lateral strike-slip events occurring on 29 December 2019 and 06 January 2020, at depths of ∼9 and ∼11 km, respectively, and would produce positive coulomb stress changes in the region of the M_w 6.4 hypocenter (Fig. S4).

The M_w 6.4 mainshock occurred on 7 January 2020, ∼10.5 km south of the town of Guayanilla, Puerto Rico at a depth of 15.9 km (using relocation) and showed the progression of the sequence from purely strike slip (Fig. S5) to an earthquake sequence characterized by both normal- and strike-slip-faulting events (Fig. 4 ternary diagram, and Fig. S6). The mainshock occurred as the result of extensional faulting with a strike and dip of 268° and 46°, respectively. Rupture area was likely greater than 130 km^2 and less than 320 km^2 (from fault-scaling relationships from Mai and Beroza, 2000 and Blaser *et al.*, 2010, respectively) with slip exceeding 1 m. Characteristic rupture areas using these fault-scaling relationships are shown in Figure 4.

Following the 7 January 2020 M_w 6.4 mainshock, rapid diversification of rupture styles and outward expansion of aftershock events away from the location of the mainshock are observed with 12 **M** 4+ events occurring on 7 January 2020 alone. This is illustrated in Figure 4 as the yellow events

Downloaded from http://pubs.geoscienceworld.org/ssa/srl/article-pdf/93/2A/544/5553020/srl-2021238.1.pdf
by USGS Library user

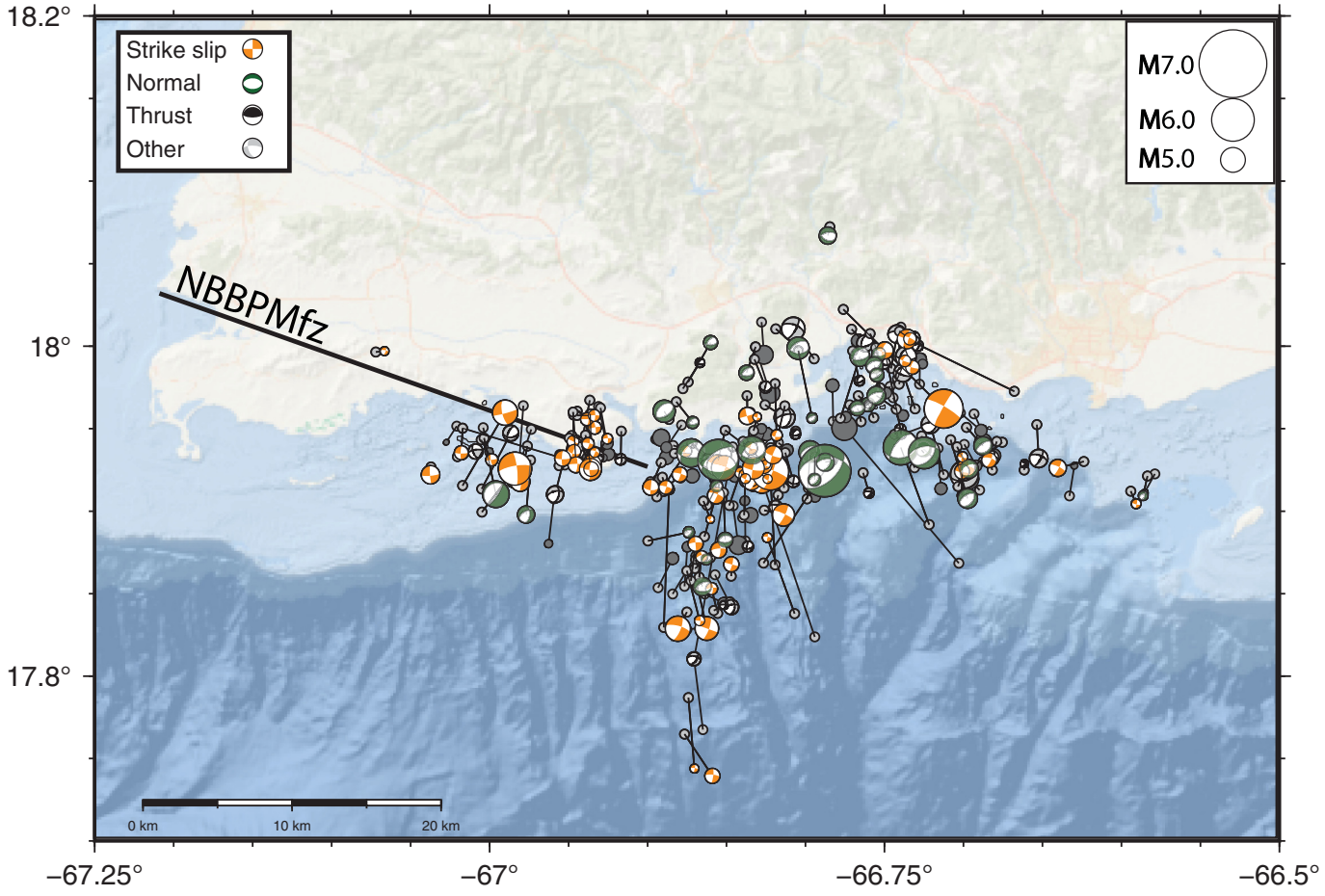


Figure 3. Illustration of calibrated relocations of 200 events from 28 December 2019 to 04 July 2020 colored as a function of mechanism type. Focal mechanisms are plotted in their relocated positions for which mechanism data are available. For which mechanisms are not available, dark-gray circles indicate relocated positions. Light-gray circles indicate locations as reported in the USGS's ComCat database. Relocation of events shows the movement of events from locations yielding no pattern to locations yielding a distinct east–west and north–south lineation of events. Faulting type for each event is determined using methods from Frohlich (1992) and (2001). The NBBPMfz is shown in black. Location of the NBBPMfz from Roig-Silva *et al.* (2013). Focal mechanisms and original locations from the USGS ANSS ComCat.

show a higher degree of variability in their ternary diagram and geographic distributions. Prior to the mainshock, distributions of earthquakes show little variability with most foreshocks occurring near the location of the mainshock. Immediately following the M_w 6.4 earthquake, rapid expansion of events to the north and east is seen (yellow events in Fig. 4). Accompanying this geographic expansion, there is a diversification of rupture kinematics seen as oblique normal-faulting and left-lateral and right-lateral events are distributed around the mainshock's rupture.

Seismicity following the mainshock (shown as orange events in Fig. 4) shows continued outward spread, predominantly to the south and west. Directly to the west of the location of the mainshock and within the mainshock's likely rupture area, three **M** 5+ normal-faulting events, including the largest aftershock, the 11 January 2020 M_w 5.9 occurred. Additional events which occurred near the north and south of the mainshock's rupture zone show right-lateral slip along the north–northeast trend and likely occurred on a fault conjugate to the NBBPMfz (M. Blasweiler *et al.*, unpublished manuscript, see Data and Resources). These strike-slip events occur within and south of the rupture area of the mainshock.

Later events, shown in dark orange and red (Fig. 4), occurred to the west and northwest of and outside of the mainshock's rupture area. Choosing the west–southwest-oriented nodal planes (for consistency with the seismicity trend), these earthquakes indicate left-lateral strike-slip motion. These left-lateral events occur in a linear trend which intersects the north–northeast-trending events at an oblique angle. In addition, these left-lateral events have dip values between 80° and 90°, with rakes less than 30°. Oblique faulting is more common along the west–southwest-trending sequence (oblique motion shown as gray vectors in Figs. S5 and S6) in contrast to the north–northeast structure and may be indicative of a minor component of extension existing along the west–northwest structure.

Downloaded from http://pubs.geoscienceworld.org/ssa/srl/article-pdf/93/2A/544/5553020/srl-2021238.1.pdf
by USGS Library user

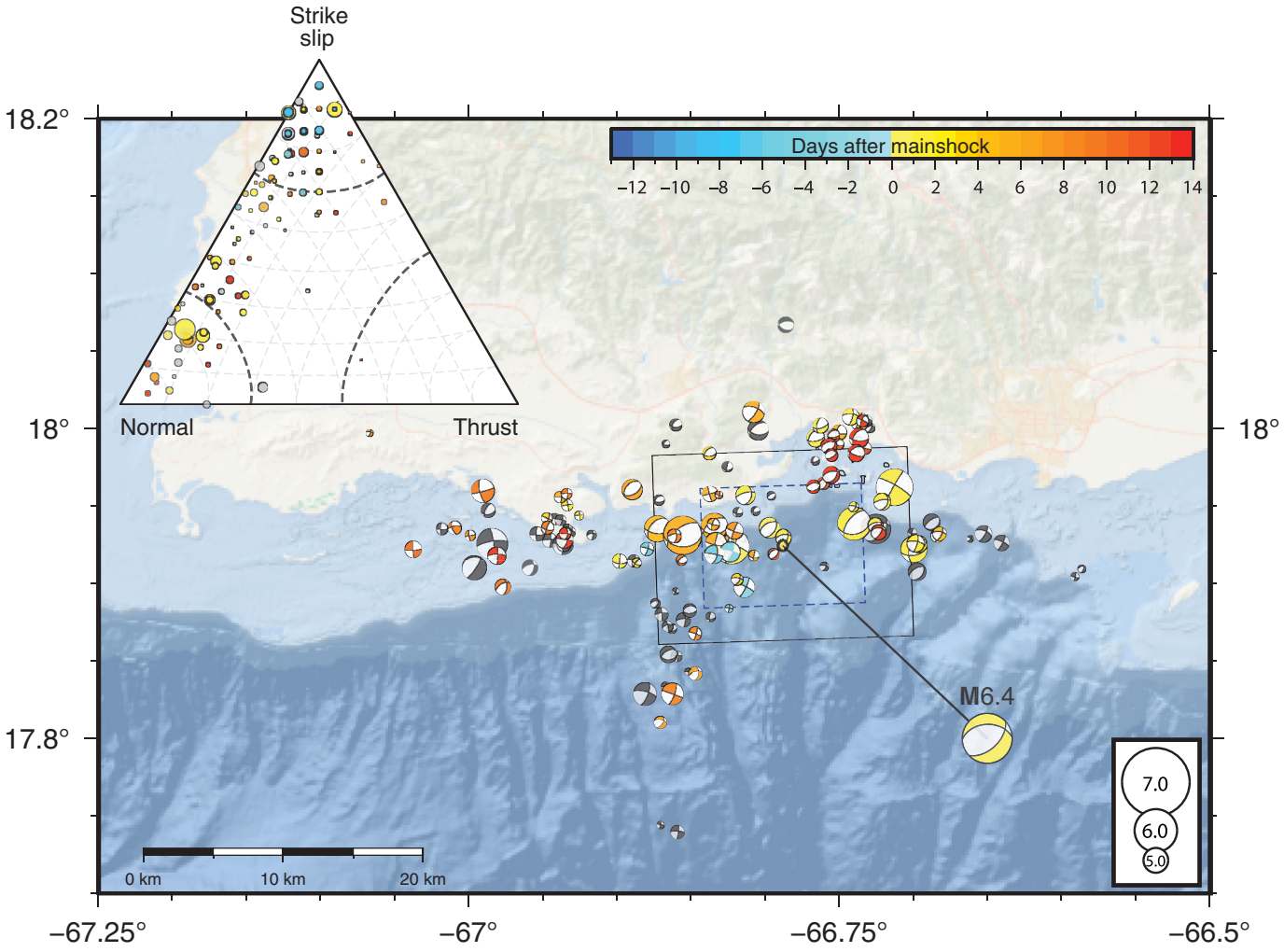


Figure 4. Focal mechanisms and ternary diagram plotted as a function of time relative to the 7 January 2020 M_w 6.4 mainshock. Colors diverge from cool colors prior to the date of the mainshock to warmer colors following the mainshock with gray events indicating events occurring later in 2020. Prior to the mainshock, all events yield strike-slip rupture as shown on the ternary diagram. Following the mainshock, rupture styles rapidly diversify to incorporate normal, strike-slip, and oblique events. Square boxes show endmember mainshock rupture areas using methods from Mai and Beroza (2000) (blue-dashed box) and Blaser *et al.* (2010) (solid-black box). Focal mechanisms from the USGS ANSS ComCat.

Discussion

The availability of these calibrated relocations for the earthquakes in the SWPRSS allows us to gain insight into the spatial and temporal distributions of earthquakes when compared to the single event locations. As seen in Figure 3, the calibrated relocations show a systematic shift of locations to the north and closer to land as compared to the single event locations. The relocation of events east of 66.9°W produces a clustering of events closer to the 7 January 2020 mainshock. The clustering of events near the M_w 6.4 mainshock's location implies that many of the normal faulting earthquakes are relocated within the mainshock's fault area (shown in Fig. 4). In addition, smaller strike-slip events, originally occurring east of ~66.9°W and north of ~17.95°, were relocated further north and form a linear trend of events in an north–northeast orientation. Events originally west of 66.9°W relocate further south. These events are relocated further offshore and collapse into a linear trend that is oriented west–southwest and are well aligned with the orientation of the NBBPMfz (Fig. 5 map).

After event relocation, the SWPRSS shows three kinematically distinct structures: (1) A north–northeast-trending structure of right-lateral strike-slip earthquakes, (2) A west–southwest-trending structure hosting oblique events intermediate between strike-slip and normal-faulting events, and left-lateral strike-slip events, and (3) An east–west lineation and clustering of extensional faulting which is oriented obliquely to and beneath both strike-slip structures.

The north–northeast-trending structure that hosts right-lateral earthquakes is clearly seen in Figures 4 and 5 and is active throughout the sequence. This linear trend of similar events extending from 10 to 22 km in depth appears to reflect a

Downloaded from http://pubs.geoscienceworld.org/ssa/srl/article-pdf/93/2A/544/5553020/srl-2021238.1.pdf
by USGS Library user

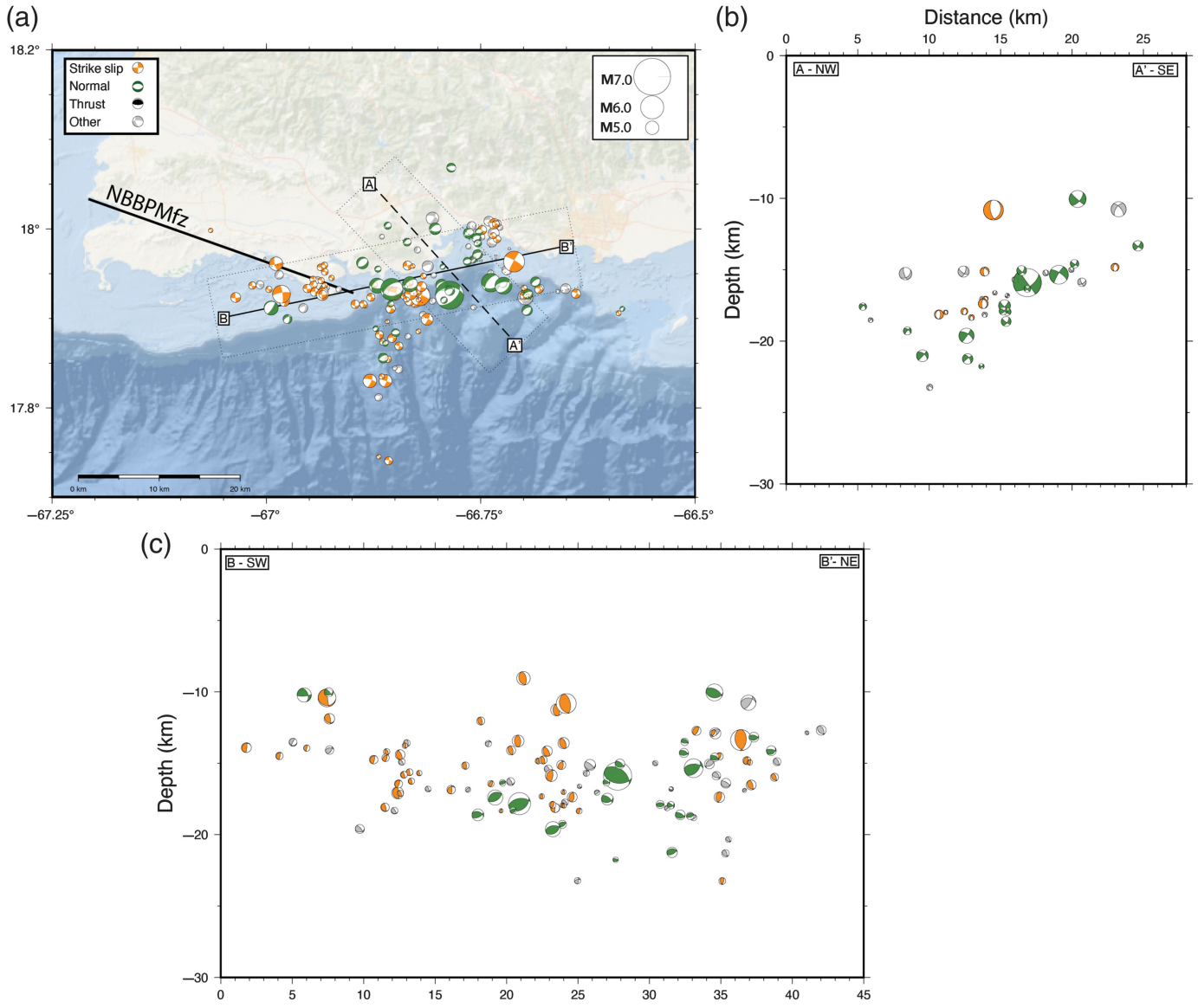


Figure 5. (a) Focal mechanisms plotted as a function of rupture style. The NBBPMfz is shown in black. (b) A–A′ profile illustrates a sequence of deepening normal-faulting events to the west–northwest. Preferred nodal planes of normal faulting events align with west–northwest dip of normal-faulting events. In addition, A–A′ profile shows vertically dipping strike-slip events occurring shallower and above and west–northwest-dipping normal-faulting sequence indicating a vertically dipping fault hosting strike-slip motion. (c) B–B′ profile shows west-dipping sequence of normal-faulting events occurring deeper than strike-slip faults. B–B′ line intersects north–northeast-trending lineations and shows vertically dipping strike-slip events at ~25 km indicative of a north–northeast-trending strike-slip fault. Location of the NBBPMfz from Roig-Silva *et al.* (2013). Focal mechanisms from the USGS ANSS ComCat.

strike-slip fault that lies above and crosscuts the rupture area of M_w 6.4 mainshock. As seen in the A–A′ cross section in Figure 5b, these strike-slip events appear to terminate at depth along the M_w 6.4 normal-faulting plane. The temporal distribution of earthquakes along the north–northeast fault suggests that it ruptured during the 06 January 2020 M_w 5.7 and the 29 December 2019 **M** 5 events as well as other smaller events prior to the mainshock. In addition, Coulomb stress modeling shows that events occurring along this north–northeast fault could increase relevant stresses in the fault plane of the 7 January 2020 mainshock.

The west–southwest-trending system of earthquakes contains primarily left-lateral strike-slip events and oblique events with similarly oriented fault planes. We interpret the alignment of left-lateral events as a west–southwest-oriented fault system that obliquely intersects the mainshock's area of rupture and continues to the east of the mainshock. The orientation and sense of motion along the west–southwest-oriented fault system is consistent with the onshore NBBPMfz and may indicate that these left-lateral events are the result of slip along the eastern portion of the NBBPMfz (M. Blasweiler *et al.*, unpublished manuscript, see Data and Resources). The higher

Downloaded from http://pubs.geoscienceworld.org/ssa/srl/article-pdf/93/2A/544/5553020/srl-2021238.1.pdf
by USGS Library user

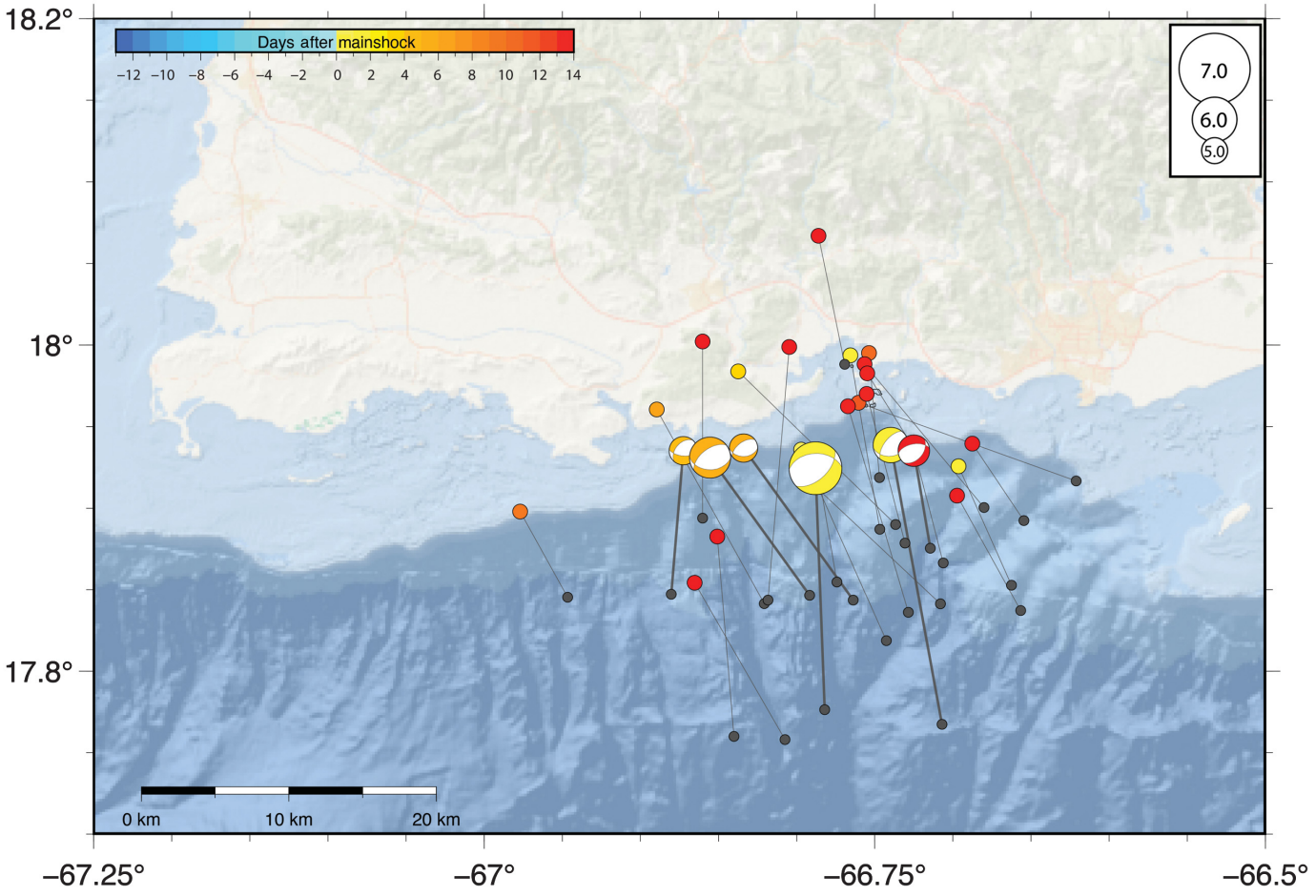


Figure 6. Focal mechanisms show **M** 5+ relocated events with colored dots showing **M** 4+ events colored as a function of time. Dark-gray circles show events projected to the surface along dip direction. Surface projections show the clustering of events along two east–west-trending bathymetric features. Focal mechanisms from the USGS ANSS ComCat.

number of oblique events and presence of normal faulting along the west–southwest-fault system suggests this structure also accommodates some amount of extensional deformation. In addition, the west–southwest-fault system shows vertically dipping strike-slip events extending from ~10 to 22 km in depth (Fig. 5 A–A′ cross sections).

North–northeast and west–southwest strike-slip fault systems both intersect obliquely within the mainshock's likely rupture area. Here, normal-faulting events occur progressively further from the mainshock over time. We interpret the outward expansion of extensional events away from the mainshock to be the result of normal-faulting events occurring along the west–northwest-dipping plane of the mainshock accommodating extension outside the initial rupture area.

Although in map view normal-faulting events form less apparent lineations than strike-slip events discussed earlier, the alignment of normal-faulting events onto linear structures at depth (Fig. 5 A–A′ and B–B′ profiles) events are indicative of extensional faulting events along a coherent northwest-dipping structure. Cross sections (Fig. 5) show a west–northwest deepening of normal-faulting events beneath both the west–southwest and north–northeast strike-slip structures. The occurrence of normal-faulting events almost exclusively along this structure as well as the alignment of these earthquakes' fault planes (Fig. 5, A–A′) argue for the presence of a significant north–northwest-dipping normal fault in southwest Puerto Rico and is consistent with the mean *T*-axis orientation determined in M. Blasweiler *et al.* (unpublished manuscript, see Data and Resources).

Surface projection of these normal-faulting events along dip direction shows the intersection of surface projections along two east–west-oriented bathymetric features south of the island of Puerto Rico (Fig. 6). Consistent faulting geometries within these events, increasing earthquake depths to the west–northwest (Fig. 5b,c), and surface projection all indicate that the SWPRSS extensional events occurred primarily along two east–west-trending planes that dip to the northwest beneath Puerto Rico and intersect the seafloor along two prominent bathymetric features south of the island.

Downloaded from http://pubs.geoscienceworld.org/ssa/srl/article-pdf/93/2A/544/5553020/srl-2021238.1.pdf
by USGS Library user

Tectonic Implications

These absolute relocations for the SWPRSS allow us to utilize the different suites of events and place events into a revised tectonic setting for the southern margin of Puerto Rico. As noted earlier, the tectonic relationship of the Puerto Rico crustal block to the CA plate has had various interpretations. One key result from this earthquake sequence is that there are two sets of interacting fault systems—(a) a shallow, multi-segment system of strike-slip faults that lie in the upper block of a (b) larger low-angle normal fault system that hosted the mainshock in the sequence (Fig. 5).

Our improved locations indicate that several of the left-lateral strike-slip events, which occur along the west–southwest-trending sequence of events, have a similar sense of motion and orientation to the onshore NBBPMfz (Fig. 5a). This implies that these strike-slip events may have occurred along the eastern extent of the NBBPMfz (M. Blasweiler *et al.*, unpublished manuscript, see Data and Resources). In addition, recent work shows that these strike-slip events may have produced coulomb stresses that positively loaded the area surrounding the M_w 6.4 mainshock (Fig. S4) (M. Blasweiler *et al.*, unpublished manuscript, see Data and Resources). This implies that strike-slip events occurring along the eastern extent of the NBBPMfz may be capable of triggering **M** 6+ earthquakes along larger extensional fault systems to the east of the NBBPMfz and south of Puerto Rico.

This improved set of earthquake locations and the set of moment tensor solutions for the larger normal-faulting events allow us to project the fault planes of the events to the surface and infer in which they would crop out (if they ruptured to the surface). What we find (Fig. 6) is that the normal-faulting events project to two linear terrace-like features along the shelf south of Puerto Rico. In particular, the mainshock and several of the aftershocks all, when projected, daylight along a prominent shelf along the margin. The other normal-faulting events projects to a second linear figure at shallower depth, and closer to the coast.

We interpret these results to indicate that the fault system that hosted the M_w 6.4 mainshock is a major, active fault that has hosted numerous past events, to produce the observed seafloor morphology. Other, also long-lived, structures hosted many of the aftershocks and appear to be subparallel faults associated with the main normal fault. This sequence of events and the strong correlation of the main fault structure that hosted the M_w 6.4 earthquake along with the submarine morphology argue that extensional (normal) faulting is a major contributor to the tectonic evolution of the southern margin of Puerto Rico. Based on the regional extent (>130 km) of the corresponding linear feature in the seafloor morphology, this implies that events such as the M_w 6.4 mainshock could be major contributors to future earthquake hazard in southern Puerto Rico. The geographic extent also implies that events larger than the M_w 6.4 earthquake are possible.

Conclusion

Utilizing calibrated earthquake relocations of the 2019–2020 Puerto Rico earthquake sequence, we have produced a catalog of 200 relocated events that reveal in better detail structures with implications for potential seismic hazards offshore of southwest Puerto Rico. Our new relative relocations show the organization of earthquakes into three clusters of events, each with distinct kinematic and temporal characteristics. We interpret these clustering of events as three separate structures: A north–northeast-trending right-lateral fault, a distributed zone of normal-faulting earthquakes in the mainshock's rupture area, and a more western west–southwest-trending left-lateral fault. In addition, we show that extensional events may have occurred along a pre-existing structure, which intersects the seafloor and that the M_w 6.4, may have resulted from positive coulomb stresses from foreshocks occurring along the eastern extent of the NBBPMfz. The relocation of earthquakes in Puerto Rico has provided new insight into the tectonic structure southwest of the island and provided an illustration of the importance of accurate earthquake relocations.

Data and Resources

Any use of trade, product, or firm names is for descriptive purposes only and does not imply endorsement by the U.S. Government. Initial earthquake locations and associated phase reading used in this study were obtained from the International Seismological Centre (ISC) Bulletin of which National Earthquake Information Center (NEIC) is a contributor. Most of the local and regional phase picks were determined by NEIC and/or the Puerto Rico seismic network. Events were obtained using search parameters of a radius of 50 km from the 7 January 2020 M_w 6.4 U.S. Geological survey (USGS) NEIC location from 28 December 2019 to 04 July 2020.

Moment tensor data were obtained by searching the USGS Comprehensive Earthquake Catalog (ComCat) (U.S. Geological Survey, Earthquake Hazards Program, 2017) using the libcomcat tool (Hearne, 2020). The resultant Indios, Puerto Rico, calibrated relocations presented in this study can be found in Benz (2021).

Plots were made using the Generic Mapping Tools version v.6.2.0 (Wessel *et al.*, 2019). The unpublished manuscript by M. Blasweiler, M. Herman, F. Houtsma, and S. Govers, "Tectonic context and possible triggering of the 2019–2020 Puerto Rico earthquake sequence", was submitted to *Seismol. Res. Lett.* Focus section.

Supplemental material for this article includes histograms for travel-time residuals (Fig. S1), global distributions of seismic stations used in relocations (Fig. S2), histograms of confidence ellipses (Fig. S3), coulomb stress models for the 2 largest foreshocks (Fig. S4), rose diagrams of earthquake slip vectors (Figs. S5 and S6), and an animation (Animation A1) showing movement of events from their original to their relocated positions.

Declaration of Competing Interests

The authors acknowledge that there are no conflicts of interest recorded.

Downloaded from http://pubs.geoscienceworld.org/ssa/srl/article-pdf/93/2A/544/5553020/srl-2021238.1.pdf
by USGS Library user

Acknowledgments

The authors would like to thank Paul Earle, Jordane Corbeau, and an anonymous reviewer for their comments and insightful suggestions.

References

Benz, H. M. (2021). Global catalog of calibrated earthquake locations, *U.S. Geological Survey Data Release*, doi: 10.5066/P95R8K8G.

Blaser, L., F. Krüger, M. Ohrnberger, and F. Scherbaum (2010). Scaling relations of earthquake source parameter estimates with special focus on subduction environment, *Bull. Seismol. Soc. Am.* **100,** no. 6, 2914–2926, doi: 10.1785/0120100111.

Byrne, D., G. Suarez, and W. McCann (1985). Muertos trough subduction—Microplate tectonics in the northern Caribbean? *Nature* **317,** 420–421, doi: 10.1038/317420a0.

Clinton, J. F., G. Cua, V. Huérfano, C. G. von Hillebrandt-Andrade, and J. M. Cruzado (2006). The current state of seismic monitoring in Puerto Rico, *Seismol. Res. Lett.* **77,** no. 5, 532–543, doi: 10.1785/gssrl.77.5.532.

DeMets, C., R. G. Gordon, and D. F. Argus (2010). Geologically current plate motions, *Geophys. J. Int.* **181,** no. 1, 1–80, doi: 10.1111/j.1365-246X.2009.04491.x.

Dolan, J. F., H. T. Mullins, and D. J. Wald (1998). *Active Tectonics of the North-Central Caribbean: Oblique Collison, Strain Partitioning, and Opposing Subducted Slabs*, Geological Society of America, Special Paper 326, 1–9, doi: 10.1130/0-8137-2326-4.1.

Frohlich, C. (1992). Triangle diagrams: Ternary graphs to display similarity of earthquake focal mechanisms, *Phy. Earth Planet. Int.* **75,** no. 3, 193–198, doi: 10.1016/0031-9201(92)90130-N.

Frohlich, C. (2001). Display and quantitative assessment of distributions of earthquake focal mechanisms, *Geophys. J. Int.* **144,** no. 2, 300–308.

Gaudreau, É., E. Nissen, E. A. Bergman, H. M. Benz, F. Tan, and E. Karasözen (2019). The August 2018 Kaktovik earthquakes: Active tectonics in northeastern Alaska revealed with InSAR and seismology, *Geophys. Res. Lett.* **117,** no. 4, B03401–B03409, doi: 10.1029/2019GL085651.

Granja Bruña, J. L., U. S. Ten Brink, A. Carbó-Gorosable, A. Muño-Martín, and M. Gómez Ballseteros (2009). Morphotectonics of the central Muertos thrust belt and Muertos trough (northeastern Caribbean), *Mar. Geol* **263,** no. 1–4, 7–33, doi: 10.1016/j.margeo.2009.03.010.

Hayes, G. P., L. Rivera, and H. Kanamori (2009). Source inversion of the W-phase: Realtime implementation and extension to low magnitudes, *Seismol. Res. Lett.* **80,** no. 5, 817–822, doi: 10.1785/gssrl.80.5.817.

Hearne, M. (2020). libcomcat, *U.S. Geological Survey Software Release*, doi: 10.5066/P91WN1UQ.

Herrmann, R. B., H. Benz, and C. J. Ammon (2011). Monitoring the earthquake source process in North America, *Bull. Seismol. Soc. Am.* **101,** no. 6, 2609–2625, doi: 10.1785/0120110095.

Jansma, P. E., and G. S. Mattioli (2005). *GPS Results from Puerto Rico and the Virgin Islands: Constraints on Tectonic Setting and Rates of Active Faulting*, Geological Society of America, Special Paper 385, 13–30, doi: 10.1130/0-8137-2385-X.13.

Kennett, B. L. N., E. R. Engdahl, and R. P. Buland (1995). Constraints on seismic velocities in the Earth from traveltimes, *Geophys. J. Int.* **122,** no. 1, 108–124, doi: 10.1111/j.1365-246X.1995.tb03540.x.

Mai, M. P., and G. C. Beroza (2000). Source scaling properties from finite-fault-rupture models, *Bull. Seismol. Soc. Am.* **90,** no. 3, 604–614, doi: 10.1785/0119990126.

Mann, P., E. Calais, J. Ruegg, C. DeMets, P. Jansma, and G. Mattioli (2002). Oblique collision in the northeastern Caribbean from GPS measurements and geological observations, *Tectonics* **21,** no. 6, 1057, doi: 10.1029/2001TC001304.

McCann, W. R. (1985). On the earthquake hazards of Puerto Rico and the Virgin Islands, *Bull. Seismol. Soc. Am.* **75,** no. 1, 251–262, doi: 10.1785/BSSA0750010251.

Mueller, C., A. Frankel, M. Peterson, and E. Leyendecker (2010). New seismic hazard maps for Puerto Rico and the U.S. Virgin Islands, *Earthq. Spectra* **26,** no. 1, 169–185, doi: 10.1193/1.3631016.

Nissen, E., A. Ghods, E. Karasözen, J. R. Elliott, W. D. Barnhart, E. A. Bergman, G. P. Hayes, M. Nemati, F. Tan, *et al.* (2019). The 12 November 2017 Mw 7.3 Ezgeleh-Sarpolzahab (Iran) earthquake and active tectonics of the Lurestan Arc, *J. Geophys. Res.* **124,** no. 2, 2124–2152, doi: 10.1029/2018JB016221.

Prentice, C. S., and P. Mann (2005). *Paleoseismic Study of the South Lajas Fault: First Documentation of an Onshore Holocene Fault in Puerto Rico*, Geological Society of America, Special Paper 385, 215–222, doi: 10.1130/0-8137-2385-X.215.

Roig-Silva, C. M., E. Asencio, and J. Joyce (2013). The northwest trending north Boquerón Bay-Punta Montalva fault zone; A through going active fault system in southwestern Puerto Rico, *Seismol. Res. Lett.* **84,** no. 3, 538–550, doi: 10.1785/0220120115.

Soto Cordero, L., A. Meltzer, E. A. Bergman, M. Hoskins, J. C. Stachnik, H. Agurto Detzel, A. Alvarado, S. Beck, P. Charvis, Y. Font, *et al.* (2020). Structural control on megathrust rupture and slip behavior: Insights from the 2016 Mw 7.8 Pedernales Ecuador earthquake, *J. Geophys. Res.* **125,** no. 2, S225–S228, doi: 10.1029/2019JB018001.

Styron, R., J. García-Pelaez, and M. Pagani (2020). CCAF-DB: The Caribbean and Central American active fault database, *Nat. Hazards Earth Syst. Sci.* **20,** 831–857, doi: 10.5194/nhess-20-831-2020.

U.S. Geological Survey, Earthquake Hazards Program (2017). Advanced National Seismic System (ANSS) Comprehensive Catalog (ComCat) of earthquake events and products: Various, doi: 10.5066/F7MS3QZH.

van Gestel, J. P., P. Mann, J. F. Dolan, and N. R. Grindlay (1998). Structure and tectonics of the upper Cenozoic Puerto Rico-Virgin Islands carbonate platform as determined from seismic reflection studies, *J. Geophys. Res.* **103,** no. B12, 30,505–30,530, doi: 10.1029/98JB02341.

Wessel, P., J. F. Luis, L. Uieda, R. Scharroo, F. Wobbe, W. H. F. Smith, and D. Tian (2019). The Generic Mapping Tools version 6, *Geochem. Geophys. Geosyst.* **20,** no. 11, 5556–5564, doi: 10.1029/2019GC008515.

Manuscript received 26 August 2021
Published online 8 December 2021

Downloaded from http://pubs.geoscienceworld.org/ssa/srl/article-pdf/93/2A/544/5553020/srl-2021238.1.pdf
by USGS Library user